

Panacea: Novel DNN Accelerator using Accuracy-Preserving Asymmetric Quantization and Energy-Saving Bit-Slice Sparsity

Dongyun Kam[†], Myeongji Yun[†], Sunwoo Yoo[†], Seungwoo Hong[†], Zhengya Zhang[‡], and Youngjoo Lee[†]
 Pohang University of Science and Technology (POSTECH)[†], University of Michigan[‡]
 {rkaehddb, mjun01, swyoo23, seungwoohong, youngjoo.lee}@postech.ac.kr[†], zhengya@umich.edu[‡]

Abstract—Low bit-precisions and their bit-slice sparsity have recently been studied to accelerate general matrix-multiplications (GEMM) during large-scale deep neural network (DNN) inferences. While the conventional symmetric quantization facilitates low-resolution processing with bit-slice sparsity for both weight and activation, its accuracy loss caused by the activation’s asymmetric distributions cannot be acceptable, especially for large-scale DNNs. In efforts to mitigate this accuracy loss, recent studies have actively utilized asymmetric quantization for activations without requiring additional operations. However, the cutting-edge asymmetric quantization produces numerous nonzero slices that cannot be compressed and skipped by recent bit-slice GEMM accelerators, naturally consuming more processing energy to handle the quantized DNN models.

To simultaneously achieve high accuracy and hardware efficiency for large-scale DNN inferences, this paper proposes an Asymmetrically-Quantized bit-Slice GEMM (AQS-GEMM) for the first time. In contrast to the previous bit-slice computing, which only skips operations of zero slices, the AQS-GEMM compresses frequent nonzero slices, generated by asymmetric quantization, and skips their operations. To increase the slice-level sparsity of activations, we also introduce two algorithm-hardware co-optimization methods: a zero-point manipulation and a distribution-based bit-slicing. To support the proposed AQS-GEMM and optimizations at the hardware-level, we newly introduce a DNN accelerator, *Panacea*, which efficiently handles sparse/dense workloads of the tiled AQS-GEMM to increase data reuse and utilization. *Panacea* supports a specialized dataflow and run-length encoding to maximize data reuse and minimize external memory accesses, significantly improving its hardware efficiency. Numerous benchmark evaluations show that *Panacea* outperforms existing DNN accelerators, e.g., $1.97\times$ and $3.26\times$ higher energy efficiency, and $1.88\times$ and $2.41\times$ higher throughput than the recent bit-slice accelerator *Sibia* and the SIMD design, respectively, on OPT-2.7B, while providing better algorithm performance with asymmetric quantization.

I. INTRODUCTION

Large-scale deep neural networks (DNNs) have been employed as powerful solutions for a variety of practical applications, including image classification [1]–[3], natural language processing (NLP) [4]–[9], AR/VR [10], and robotics [11]. However, their extensive computations and external memory accesses (EMA) result in poor throughput and increased energy consumption during inferences [12]–[15], leading to more significant challenges for a large-scale DNN’s deployment on resource-constrained edge devices [16], [17].

To address these challenges, recent works [33]–[48] have developed energy-efficient DNN inference accelerators by employing algorithm-hardware co-optimization techniques such as weight pruning [33]–[40] and quantization [41]–[49].

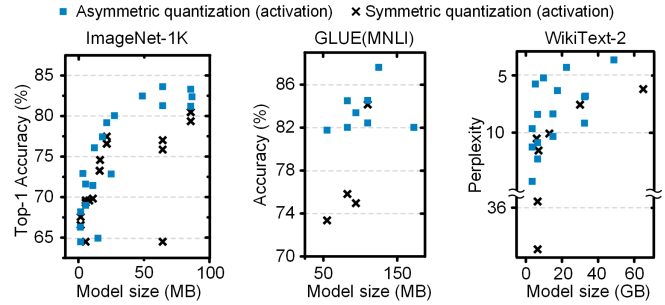


Fig. 1. Accuracy comparison on recent works utilizing symmetric [18]–[22] and asymmetric quantization [23]–[32] for activations in large-scale DNNs.

Among these techniques, low bit-precision post-training quantization (PTQ) [43]–[47] stands out by significantly lowering the complexity of operations and memory accesses, even without necessitating costly fine-tuning with large datasets. This results from enabling integer general matrix-multiplications (GEMMs) by quantizing weights and activations. However, PTQ-based methods, e.g., symmetric and asymmetric quantization, still have challenges for large-scale DNN inferences on resource-constrained devices, as summarized below.

Accuracy degradation of symmetric quantization: While symmetric quantization generally enables low bit-precisions, it can cause significant accuracy loss during large-scale DNN inferences, such as transformer models, which contain layers producing asymmetric distributions or long-tail distributions in input activation matrices [50], [51]. Recent studies at the algorithm-level [18]–[32] have addressed the accuracy degradation issue by applying symmetric quantization to weights and asymmetric quantization to activations, as illustrated in Fig. 1. Consequently, to capitalize on the large-scale model’s high accuracy fully, it is crucial to utilize low-bit asymmetric quantization for input activations.

HW optimization challenge of integer GEMMs with asymmetric quantization: However, integrating integer GEMMs with asymmetric quantization makes it difficult to utilize recent optimization techniques, such as sparsity, for energy-efficient DNN inferences [30], [52]. While integer GEMMs with symmetric quantization [53]–[56], have actively supported sparsity even for dense DNN models, which have high bit-slice sparsity ($>90\%$) in high-order slices after segmenting near-zero values into multiple bit-slices, integer GEMMs with asymmetric quantization cannot exploit the slice sparsity due to few zero

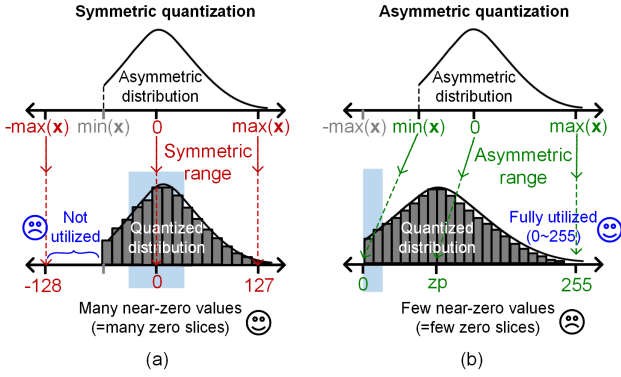


Fig. 2. Examples of uniform quantization methods: 8-bit (a) symmetric and (b) asymmetric approaches.

slices. Unlike symmetric quantization centering values around zero, as shown in Fig. 2, asymmetric quantization produces quantized distributions that are not centered around zero, generating many nonzero slices that cannot be directly compressed and skipped. Therefore, to simultaneously enhance accuracy and hardware efficiency, it is essential that a new GEMM operation and its hardware architecture efficiently address the numerous multiply-and-accumulate (MAC) operations and memory accesses associated with nonzero slices.

This paper proposes the first asymmetrically-quantized bit-slice DNN accelerator, *Panacea*, successfully achieving high accuracy and hardware efficiency for resource-limited devices. The contributions of *Panacea* are summarized as follows:

- The **Asymmetrically-Quantized bit-Slice GEMM (AQS-GEMM)** is newly developed to compress high-order nonzero slices, which are frequently observed in asymmetric quantization, and skip MAC operations of compressed slices. To get exact GEMM results, the AQS-GEMM efficiently computes a compensation term for skipping compressed slices, while reusing loaded data and minimizing additional memory accesses. It finally reduces the number of MAC operations by 61% compared to the dense GEMM, enabling bit-slice sparsity.
- To increase high-order (HO) slice sparsity in activations, *Panacea* utilizes two algorithm-hardware co-optimization methods: **Zero-Point Manipulation (ZPM)** and **Distribution-based Bit-Slicing (DBS)**. They are activated during the PTQ calibration (algorithm-level) and exploit higher sparsity during inferences (hardware-level). The ZPM properly adjusts the zero-point value of activation to put more quantized values into a slice skip range, thereby increasing the HO slice sparsity by at most 33%p. To further increase the sparsity, the DBS categorizes quantized distributions into three types during the calibration. Based on the identified types, the DBS applies different bit-slicing rules to different layers during the inference step by using low-cost shifting units, increasing the HO slice sparsity by at most 56%p and overall energy efficiency by 10.1% for DeiT-base.
- *Panacea* efficiently computes the AQS-GEMM with the run-length encoded bit-slices, reducing the number of

MAC operations and EMA. Its processing elements maximize data reuse by dedicating sparse and dense workload operators, which are activated in parallel, further reducing on-chip memory accesses. The processing elements' compensator also reuses the loaded weight slices to compensate for the skipped MAC operations, producing exact GEMM results with negligible overhead. To address the low utilization problem of resources at high slice sparsity, *Panacea* adopts a double-tile processing flow that allocates additional computation workload into free operators in each processing element.

We evaluate the hardware-level performance of *Panacea* on different design parameters, such as the number of operators, and different slice sparsities of weights and activations. In addition, to properly determine *Panacea*'s design options, we analyze the slice sparsity for large-scale DNN benchmark models. Our evaluations demonstrate that *Panacea* outperforms recent dense DNN accelerators: the systolic array [57], [58], the SIMD [59], and the bit-slice accelerator *Sibia* [53]. Compared to *Sibia* [53], which only supports symmetric quantization, *Panacea* improves energy efficiency by 2.03 \times , 1.97 \times , 1.52 \times , and 1.49 \times and throughput by 1.34 \times , 1.88 \times , 1.24 \times , and 1.37 \times for GPT-2 [7], OPT-2.7B [60], Llama-3.2-1B [61], and ResNet-18 [1], respectively, by efficiently utilizing high slice sparsity, while providing better accuracy with asymmetric quantization. The results also show *Panacea* outperforms *Sibia* for OPT-2.7B [60] using 4-bit weights.

II. BACKGROUND & MOTIVATION

A. Quantization and integer GEMM

Uniform Quantization. Quantization plays a pivotal role in reducing the computational cost and memory footprint by enabling computations with low bit-precision [30], [41]–[47], [49], [62]–[68]. There are two uniform quantization techniques: symmetric and asymmetric quantization schemes, which usually use signed and unsigned integers, respectively. Given an input matrix \mathbf{x} , two schemes are computed as follows:

$$\mathbf{x}_{\text{int}b} = Q(\mathbf{x}; s, b) = \text{clip}\left(\left\lfloor \frac{\mathbf{x}}{s} \right\rfloor; -2^{b-1}, 2^{b-1} - 1\right), \quad (1)$$

$$\mathbf{x}_{\text{uint}b} = Q(\mathbf{x}; s', zp, b) = \text{clip}\left(\left\lfloor \frac{\mathbf{x}}{s'} \right\rfloor + zp; 0, 2^b - 1\right), \quad (2)$$

where quantization parameters are defined as the scale factors $s = 2 \times \max(|\mathbf{x}|)/(2^b - 1)$, $s' = (\max(\mathbf{x}) - \min(\mathbf{x}))/ (2^b - 1)$, the bit-width b , and the b -bit zero-point $zp = \text{clip}(\lfloor -\min(\mathbf{x})/s' \rfloor; 0, 2^b - 1)$. Essentially, in symmetric quantization, the positive and negative ranges of a value are symmetrically mapped to the positive and negative sides of the quantized space [30], [68], as shown in Fig. 2(a). This often leads to underutilization of part of the quantized space, like in common scenarios of DNN computation where the negative quantized space is not fully utilized. On the other hand, asymmetric quantization maps the entire value range to the unsigned quantized space, mapping the zero value into zp that no longer centers the quantized space but instead varies based on the range of the value [30], [68], as shown in Fig. 2

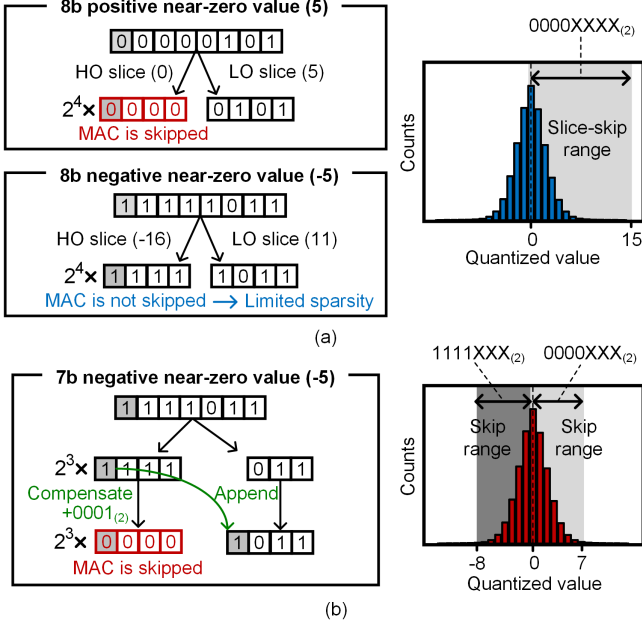


Fig. 3. (a) the straightforward bit-slice representation [54], and (b) the signed bit-slice representation [53].

(b). This form of quantization provides the best representation of the value for a given bit-width, accommodating the actual data distribution more flexibly. Using a unique zero-point value for an input matrix enhances the precision with which distribution characteristics are captured, thus reducing the effects of precision loss [23]–[32].

Post-Training Quantization. PTQ quantizes weights and input activations without the costly fine-tuning and any labeled dataset. This method only necessitates a minimal calibration dataset, typically a subset of the training dataset [69]. During the calibration, this subset is fed into a DNN model to calculate each layer’s scale factor and zero point [69]. Consequently, PTQ offers an efficient and rapid quantization approach, which is especially beneficial for the varied landscape of DNN architectures. In this paper, we consistently apply PTQ across all weights and input activations.

Integer GEMM with asymmetric quantization. Large-scale DNNs often incorporate a lot of computationally intensive GEMMs [67]. Quantizing weights and activations in all layers makes it possible to employ low-bit integer GEMMs, resulting in significantly enhancing hardware efficiency. To minimize accuracy degradation caused by the PTQ without additional computational overhead, one effective strategy is to compute GEMMs with symmetric weight quantization and asymmetric activation quantization [30] as detailed in (3).

$$\begin{aligned}
 \mathbf{W}\mathbf{x} + \mathbf{b} &\approx s_W(\mathbf{W}_{\text{int}})s_x(\mathbf{x}_{\text{uint}} - zp_x) + \mathbf{b} \\
 &= s_W s_x(\mathbf{W}_{\text{int}}\mathbf{x}_{\text{uint}} - zp_x \mathbf{W}_{\text{int}}\mathbf{1}^{K \times 1} + \mathbf{b}_{\text{int}}) \\
 &= s_W s_x(\mathbf{W}_{\text{int}}\mathbf{x}_{\text{uint}} + \hat{\mathbf{b}}_{\text{int}}), \quad (3)
 \end{aligned}$$

where \mathbf{W} is a $M \times K$ weight, \mathbf{x} is a $K \times N$ activation, \mathbf{b} is a $M \times 1$ bias, and $\mathbf{1}^{K \times 1}$ is a $K \times 1$ vector consisting entirely of ones. The term $\mathbf{W}_{\text{int}}\mathbf{x}_{\text{uint}}$ is an integer GEMM that is mainly performed in a DNN accelerator. The second term

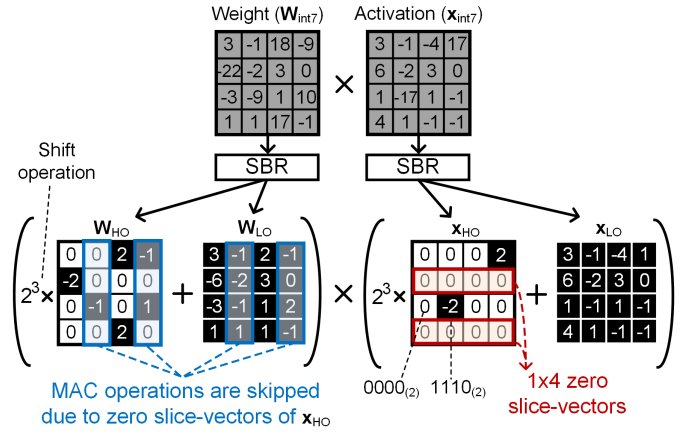


Fig. 4. An example of the bit-slice GEMM using 7-bit symmetric quantization and the SBR for both weight and activation [53].

$zp_x \mathbf{W}_{\text{int}}\mathbf{1}^{K \times 1}$ can be pre-computed and added to the bias term because it is independent on \mathbf{x}_{uint} and known in advance. Thus, computing the integer GEMMs with asymmetric quantization does not incur additional overhead during inferences.

B. Previous Bit-Slice GEMMs

To enhance hardware efficiency during dense model inferences, recent DNN accelerators [53]–[56] utilize low precision, and further mitigate the complexity of integer GEMMs by segmenting integers into bit-slices and leveraging sparsity at high-order (HO) slices. For example, as illustrated in Fig. 3(a), the straightforward bit-slicing [54] typically divides an 8-bit integer into a 4-bit signed HO slice and a 4-bit unsigned low-order (LO) slice, skipping MAC operations for $0000_{(2)}$ HO slices. However, this approach cannot skip $1111_{(2)}$ HO slices, which occur as frequently as $0000_{(2)}$ in symmetric quantization [70]–[74], limiting slice-level sparsity.

The signed bit-slice representation (SBR) [53], as shown in Fig. 3(b), has been introduced to overcome this limitation. The SBR captures zero HO slices from both positive and negative near-zero values by dividing a $(3n + 4)$ -bit integer into one 4-bit signed HO slice and n 3-bit unsigned LO slices, where n is a positive integer. Then, 3-bit unsigned LO slices are extended to 4-bit signed slices. For the case of $n = 1$ depicted in Fig. 3(b), the 3-bit LO slice is first extended to a 4-bit signed slice by appending the sign bit of the HO slice, and then $1111_{(2)}$ HO slice is added by $0001_{(2)}$ to compensate for the attached sign bit, converting it to $0000_{(2)}$. Given the enhanced slice-level sparsity, the bit-slice GEMM in [53] is designed to group v slices into a v -length slice-vector and skip operations for vectors that consist entirely of zero slices. More precisely, based on the SBR dividing a 7-bit integer value into two 4-bit slices [53], the bit-slice GEMM is calculated as

$$\mathbf{W}_{\text{int}7}\mathbf{x}_{\text{int}7} + \hat{\mathbf{b}}_{\text{int}32} = (\mathbf{W}_{\text{HO}} + \mathbf{W}_{\text{LO}})(\mathbf{x}_{\text{HO}} + \mathbf{x}_{\text{LO}}) + \hat{\mathbf{b}}_{\text{int}32}. \quad (4)$$

There are four bit-slice computations, i.e., $\mathbf{W}_{\text{HO}}\mathbf{x}_{\text{HO}}$, $\mathbf{W}_{\text{LO}}\mathbf{x}_{\text{HO}}$, $\mathbf{W}_{\text{HO}}\mathbf{x}_{\text{LO}}$, and $\mathbf{W}_{\text{LO}}\mathbf{x}_{\text{LO}}$, which are probably sparse GEMMs except for $\mathbf{W}_{\text{LO}}\mathbf{x}_{\text{LO}}$. Note that the previous bit-slice GEMM

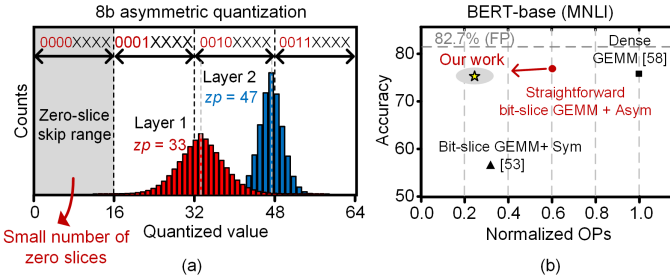


Fig. 5. (a) Distributions of asymmetrically quantized activations. (b) Accuracy comparison when using different GEMMs for BERT-base [5] and GLUE dataset (MNLI) [75].

only supports to skip the operations of zero-slice vectors related to either \mathbf{W}_{HO} or \mathbf{x}_{HO} . Fig. 4 illustrates an example of the bit-slice GEMM using 7-bit symmetric quantization alongside SBR and 4-length slice-vectors, i.e., $v = 4$. The SBR and grouping slices into vectors [53] still exploit bit-slice sparsity and effectively reduce computational complexity. However, since these methods only consider skipping operations of zero HO slices, it is impossible to exploit slice-level sparsity for asymmetric quantization, which generates few zero HO slices.

C. Motivation

Since most of the actual activations in DNN layers have an asymmetric distribution [50], [51], symmetric quantization cannot fully utilize the quantization bit-width, potentially leading to accuracy loss. To address this challenge, recent algorithm-level works have embraced asymmetric quantization, specifically for activations [23]–[32]. However, one drawback of asymmetric quantization is that it does not generate sufficient zero slices, which can be skipped in the existing bit-slice GEMMs [53]–[56], as shown in Fig. 5(a). To address this limitation, there is a clear need for a novel bit-slice GEMM approach, which skips frequent nonzero slices in asymmetrically-quantized activations, and optimization methods that increase the frequency of skippable nonzero slices. In response to this need, this paper introduces a new bit-slice GEMM along with several optimization methods and its accelerator, *Panacea*, to reduce memory accesses and the number of computations while maintaining high accuracy, as shown in Fig. 5(b).

III. PANACEA ACCELERATOR

A. Overview

Panacea is a novel DNN accelerator that supports both asymmetric quantization and sparse bit-slice computations to achieve high accuracy and energy efficiency. Fig. 6 shows an overview of the proposed work, mainly consisting of ① asymmetrically quantized bit-slice GEMM (AQS-GEMM) in *Panacea*, which enables the bit-slice GEMM for asymmetric quantization during inference (Section III-B), and optimization methods: ② zero-point manipulation (ZPM) and ③ distribution-based slicing (DBS), which increase slice-level sparsity of activations during calibration (Section III-C). The PTQ calibration quantizes weights and extracts activation’s quantization parameters, including s_x and zp_x , as outlined in

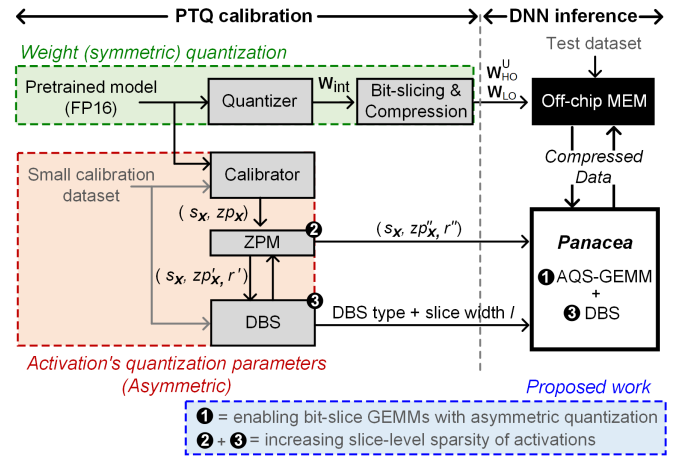


Fig. 6. Overview of PTQ calibration and DNN inference, which are based on the proposed methods and *Panacea*.

(1) and (2). The parameters are adjusted through ② ZPM and ③ DBS to enhance slice-level sparsity by considering the slice skip range of the AQS-GEMM. During inference, *Panacea* utilizes the compressed weights, symmetrically quantized during calibration, and compressed activations, asymmetrically quantized based on the parameter values obtained from calibration, for bit-slice GEMMs. ① *Panacea*’s AQS-GEMM core efficiently handles bit-slice computations by skipping not only zero slices in symmetric quantization, but also frequent nonzero slices in asymmetric quantization. Note that accumulated GEMM results, i.e., activations, are re-quantized and compressed for the next layer. In terms of hardware architecture, *Panacea* separates dynamic and static workload operators to optimize sparse and dense computations, maximizing data reuse and minimizing EMA (Section III-D).

B. AQS-GEMM

Panacea implements symmetric quantization for weights and asymmetric quantization for activations. For weight quantization, it adopts SBR [53] segmenting $(3n + 4)$ -bit weight \mathbf{W}_{int} into $(n + 1)$ 4-bit sliced matrices, while for activation quantization, it utilizes the straightforward bit-slice representation method [54], [76] segmenting $(4k + 4)$ -bit activation \mathbf{x}_{uint} into $(k + 1)$ 4-bit sliced matrices. For a good understanding, this section explains the case of $n = 1$ and $k = 1$, i.e., \mathbf{W}_{int7} and \mathbf{x}_{uint8} . To compute $\mathbf{W}_{int7}\mathbf{x}_{uint8}$, *Panacea* divides it into four bit-slice computations: $\mathbf{W}_{HO}\mathbf{x}_{HO}$, $\mathbf{W}_{LO}\mathbf{x}_{HO}$, $\mathbf{W}_{HO}\mathbf{x}_{LO}$, and $\mathbf{W}_{LO}\mathbf{x}_{LO}$.

As depicted in Fig. 5(a), asymmetric quantization creates distributions that are not centered around zero, frequently observing specific nonzero HO slices near their zero point values (zp). The floating zp for different activations complicates the implementation of bit-slice GEMMs, as it changes a frequent nonzero HO slice observed in each layer. To address these challenges and enhance computational efficiency, we propose the AQS-GEMM, which compresses out these frequent nonzero slices generated by asymmetric quantization, and skips their MAC operations.

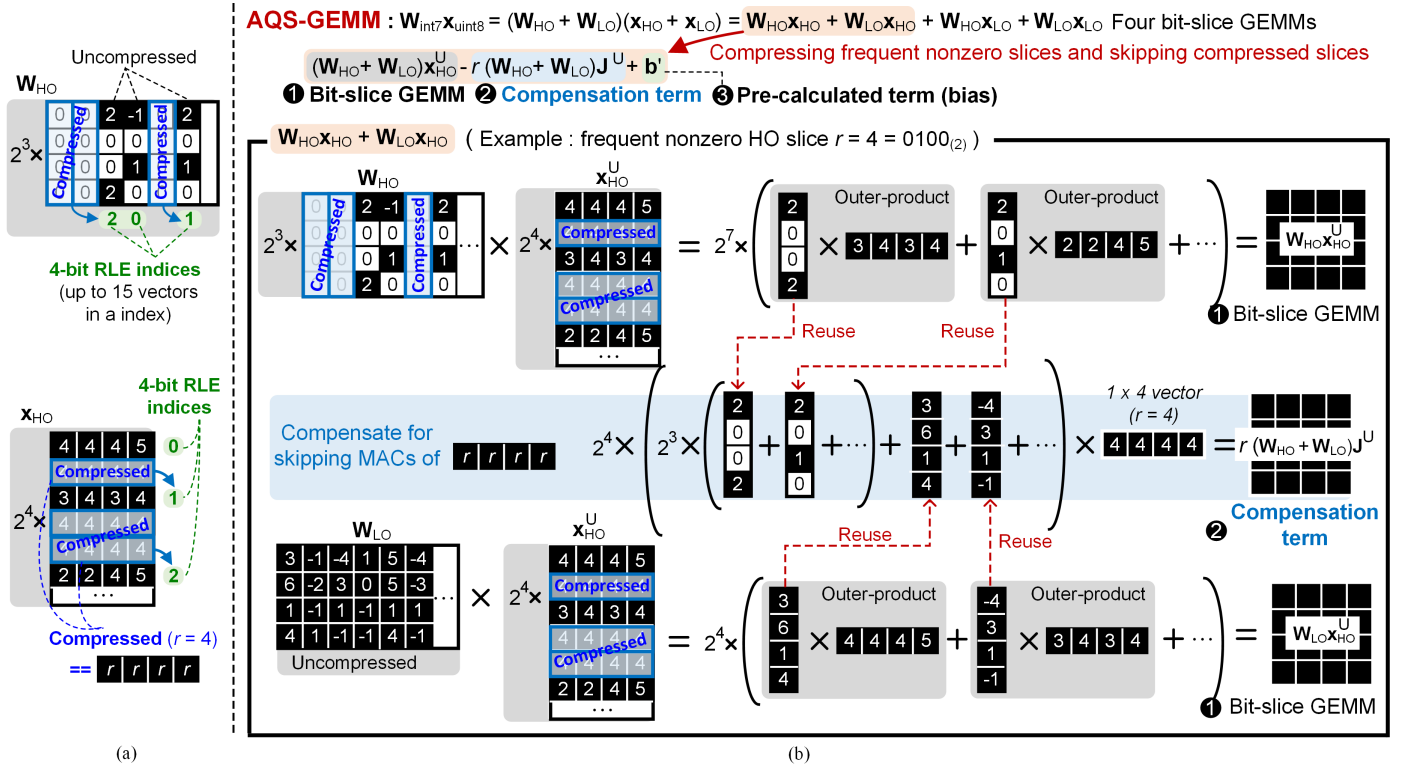


Fig. 7. (a) Compressing vectors only comprising frequent slices in \mathbf{x}_{HO} . (b) The concept of AQS-GEMM skipping MACs of compressed HO vectors.

Compressing HO slices. The AQS-GEMM operates under the assumption that HO slices are sparse and LO slices are dense. As illustrated in Fig. 7(a), the AQS-GEMM applies grouping and compression to HO slices. First, it groups \mathbf{W}_{HO} into 4×1 slice vectors and \mathbf{x}_{HO} into 1×4 slice vectors. Then, the run-length encoding (RLE) [53] is applied to the slice vectors. The RLE index bit-width denotes how many successive vectors can be compressed at a time. In the case of 4-bit RLE indices, we can compress up to 15 successive 1×4 vectors into an index. More specifically, in the case of symmetrically-quantized \mathbf{W}_{HO} , a slice-vector is compressed if all slices within the vector have zero values. For the asymmetrically-quantized \mathbf{x}_{HO} , a slice-vector is compressed if all slices in the vector are r -valued slices, where r is an HO slice of 8-bit zero point, i.e., $r = z_{p_{\text{HO}}}$. Note that many quantized values are observed around z_p due to the asymmetric quantization we applied. This results in r -values becoming predominant and others being sparse within the HO slices. With this approach, we exploit high HO vector sparsity in both weights and activations across numerous DNN layers, reducing EMA and the number of accesses from SRAM to the *Panacea's* processing engine. Our evaluation with DNN benchmarks, specifically for DeiT-base [3] on the ImageNet-1k dataset [77] and GPT-2 [7] on the WikiText-2 [75], demonstrates that compressing HO slices reduces EMA by 60.5% and 46.8%, respectively, compared to the baseline [53] using uncompressed data format from DRAM to the processing core. Furthermore, the AQS-GEMM's compression reduces SRAM access by 29.2% for

DeiT-base and 27.4% for GPT-2, compared to [53]. These reductions improve energy efficiency and mitigate the memory bandwidth demands of large-scale DNNs. In a later section, we further enhance the effect of compression by increasing slice-level sparsity followed by high vector-level sparsity.

Skipping compressed HO slice vectors. As discussed above, the \mathbf{W}_{HO} 's slice-vectors that only have zero slices, and the \mathbf{x}_{HO} 's slice-vectors that only have r -value are compressed out. This compression saves computation by skipping operations involving these compressed vectors, and it focuses computation only on the uncompressed vectors to optimize hardware efficiency. The proposed AQS-GEMM executes four bit-slice GEMMs, newly presenting a method skipping the compressed slices in the asymmetrically-quantized \mathbf{x}_{HO} as shown in Fig. 7(b). In contrast to directly skipping zero-valued slices in the previous bit-slice GEMM [53]–[56], r -valued slices in \mathbf{x}_{HO} cannot be explicitly skipped to compute exact results. To skip the compressed r -valued slices and get exact GEMM results simultaneously, the proposed method reformulates $(\mathbf{W}_{\text{HO}} + \mathbf{W}_{\text{LO}}) \mathbf{x}_{\text{HO}}$ as follows.

$$\begin{aligned}
 & (\mathbf{W}_{\text{HO}} + \mathbf{W}_{\text{LO}}) \mathbf{x}_{\text{HO}} \\
 &= (\mathbf{W}_{\text{HO}} + \mathbf{W}_{\text{LO}})(\mathbf{x}_{\text{HO}}^U + \mathbf{x}_{\text{HO}}^C) \\
 &= (\mathbf{W}_{\text{HO}} + \mathbf{W}_{\text{LO}})(\mathbf{x}_{\text{HO}}^U + r \times \mathbf{J}^C) \\
 &= (\mathbf{W}_{\text{HO}} + \mathbf{W}_{\text{LO}})(\mathbf{x}_{\text{HO}}^U + r \times (\mathbf{1}^{K \times N} - \mathbf{J}^U)) \\
 &= (\mathbf{W}_{\text{HO}} + \mathbf{W}_{\text{LO}}) \mathbf{x}_{\text{HO}}^U - r(\mathbf{W}_{\text{HO}} + \mathbf{W}_{\text{LO}}) \mathbf{J}^U + \mathbf{b}', \quad (6)
 \end{aligned}$$

where C indicates the set of compressed slices, U indicates the

TABLE I
HARDWARE WORKLOADS IN BIT-SLICE GEMM ACCELERATORS

Accel.	<i>Sibia</i> [53]		<i>Panacea</i> (AQS-GEMM core)	
	Bit-slice GEMMs	Bit-slice GEMMs w/o compensation	In (5)	In (6)
Core's comput.				
Mul.	$32K(2 - \max(\rho_x, \rho_w))$	$16K(2 - \rho_x)(2 - \rho_w)$		16
Add.	$32K(2 - \max(\rho_x, \rho_w))$	$16K(2 - \rho_x)(2 - \rho_w)$	$8K\rho_x$	$8K(1 - \rho_x)$
EMA	14K	$4K(4 - \rho_w - \rho_x)$	$8K\rho_x$	0

set of uncompressed slices, $\mathbf{x}_{\text{HO}}^{\text{C}}$ and $\mathbf{x}_{\text{HO}}^{\text{U}}$ are subset matrices of \mathbf{x}_{HO} only including compressed and uncompressed slices, respectively, and $\mathbf{J}_{\text{HO}}^{\text{C}}$ and $\mathbf{J}_{\text{HO}}^{\text{U}}$ are matrices with 1 at indices of compressed and uncompressed slices, respectively. Note that $\mathbf{x}_{\text{HO}} = \mathbf{x}_{\text{HO}}^{\text{U}} + \mathbf{x}_{\text{HO}}^{\text{C}}$, $\mathbf{x}_{\text{HO}}^{\text{C}} = r \times \mathbf{J}^{\text{C}}$ and $\mathbf{J}^{\text{C}} = \mathbf{1}^{K \times N} - \mathbf{J}^{\text{U}}$.

In (5), the case of symmetric quantization ($r = 0$) [53]–[56] becomes equivalent to $(\mathbf{W}_{\text{HO}} + \mathbf{W}_{\text{LO}})\mathbf{x}_{\text{HO}}^{\text{U}}$, which is only associated with the activation's uncompressed slices. However, in the case of asymmetric quantization ($r \neq 0$), a compensation term $(\mathbf{W}_{\text{HO}} + \mathbf{W}_{\text{LO}})(r \times \mathbf{J}^{\text{C}})$ should be added to compute the exact GEMM compared to the symmetric quantization. Unfortunately, the naive computation of compensation term requires additional memory accesses to load the weight slices associated with \mathbf{J}^{C} , which are originally skipped due to compressing \mathbf{x}_{HO} slices. The loaded weight slices for the compensation term cannot be reused, and the overhead is further exacerbated due to the increased number of compressed vectors in the case of high slice sparsity. To minimize the overhead, we derive (6) from (5), calculating the compensation term with weight slices only associated with the uncompressed slices ($\mathbf{x}_{\text{HO}}^{\text{U}}$). This enables the reuse of weight slices loaded for the bit-slice computations $(\mathbf{W}_{\text{HO}} + \mathbf{W}_{\text{LO}})\mathbf{x}_{\text{HO}}^{\text{U}}$, as shown in Fig. 7(b), accumulating the loaded weight slices and then performing an outer product with the 1×4 vector containing only r . Meanwhile, \mathbf{b}' is pre-computed offline by $(\mathbf{W}_{\text{HO}} + \mathbf{W}_{\text{LO}})(r \times \mathbf{1}^{K \times N})$, and it is added to the layer's bias in advance. As a result, with negligible overhead, the AQS-GEMM efficiently computes the bit-slice GEMM and the compensation term for exact results. Note that after decoding RLE indices to recover the original vector indices, as shown in Fig. 7(b), the bit-slice GEMM of AQS-GEMM is executed by outer products with pairs of uncompressed 4×1 weight and 1×4 activation slice-vectors that have matching indices, each of which produces 4×4 partial-sums.

Formalization of hardware workloads. Table I shows the relation between sparsity and hardware workloads, such as $4b \times 4b$ multiplications, $8b$ additions, and $4b$ EMA, in two bit-slice accelerators with sufficient memory space assumed. The workloads are formalized by the example using two bit-slices for both weights ($\mathbf{W}_{\text{int}7} \in \mathbb{Z}^{4 \times K}$) and activations ($\mathbf{x}_{\text{int}7} \in \mathbb{Z}^{K \times 4}$ for *Sibia* and $\mathbf{x}_{\text{int}8} \in \mathbb{N}^{K \times 4}$ for *Panacea*). While *Sibia* [53] only supports one of the HO vector-level sparsities of weights and activations ($\rho_w, \rho_x \leq 1$), *Panacea* accommodates both sparsities. Note that in *Sibia*, which uses symmetrically quantized activations, ρ_x represents the ratio of all-zero slice vectors, whereas in *Panacea*, it represents a broader range that includes r -valued slice vectors. Although *Panacea* requires an additional compensation term for exact

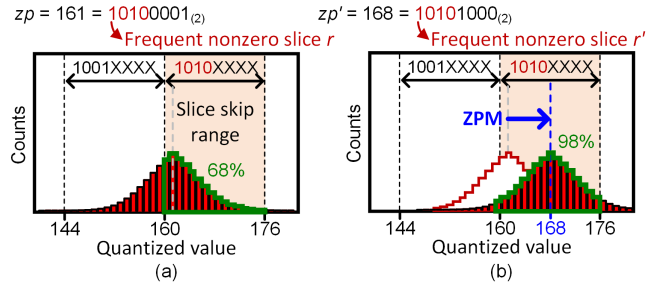


Fig. 8. Distributions of an asymmetrically quantized activation (a) without the ZPM, and (b) with the ZPM.

computations unlike *Sibia* [53], the compensation term incurs only 16 extra multiplications and low-cost additions that result in a negligible hardware overhead. In terms of EMA for bit-slice GEMMs, *Panacea* loads only the uncompressed parts, leading to lower EMA compared to *Sibia* [53], which loads dense matrices regardless of compression. The naive $8K\rho_x$ EMA overhead of the required compensation term in (5) can be eliminated by the transition to (6), which reuses the weight slices corresponding to $\mathbf{x}_{\text{HO}}^{\text{U}}$ already loaded for bit-slice GEMMs. Thus, the AQS-GEMM core in *Panacea* fully leverages the sparsities for exact computations, optimizing both computational and memory efficiency.

Scalability for lower bit-precisions. The AQS-GEMM is scalable to support any bit-width format following the $(3n+4)$ -bit weight and $(4k+4)$ -bit activation format, thereby supporting lower-bit quantization, such as 4-bit weights when $n = 0$. It is also possible to extend the idea of AQS-GEMM to either lower-bit slices. Although recent quantization works, such as OPTQ [46] and AWQ [78], have recently studied 4-bit or lower bit-precisions, they work only for weights, using 16-bit FP numbers for activations and assuming 16-bit FP multipliers. Thus, when considering low-bit quantization for both weights and activations, the 8-bit precision is still an attractive option to achieve high accuracy and hardware efficiency simultaneously.

C. Enhancing Slice-Level Sparsity

Since the AQS-GEMM achieves better efficiency thanks to the increased number of compressed vectors, increasing slice-level sparsity for both weights and activations is important. Note that improving the slice-level sparsity generally results in increased vector-level sparsity. However, activation's asymmetric quantization produces varying distributions, leading to low slice sparsity. To address this problem, we propose two algorithm-hardware co-optimization methods: zero-point manipulation (ZPM) and distribution-based slicing (DBS) within the PTQ calibration depicted in Fig. 6.

Sparsity-aware zero-point manipulation. Fig. 8(a) shows an example of asymmetric quantization leading to low sparsity at HO slices of an input activation. The example activation distribution of an FC layer in OPT-2.7B [60] is centered around the zero point $zp = 161$. When applying the compression of HO slices, the frequent HO slice becomes $r = 1010_{(2)}$, and only about 68% of total values are present in the skip range observing $1010_{(2)}$ HO slices. The actual compression ratio

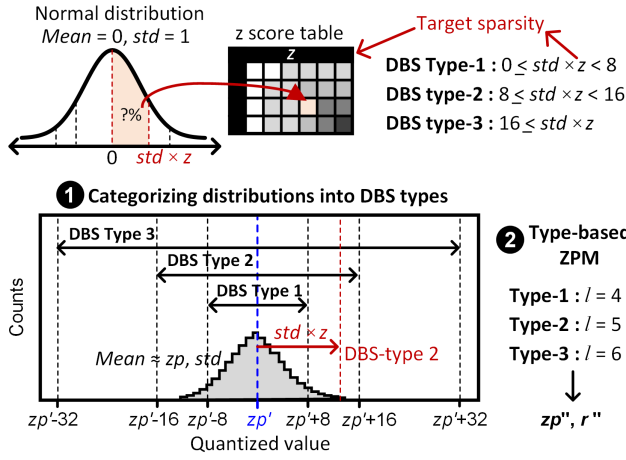


Fig. 9. Categorizing distributions of quantized activations into three types based on their standard deviations, z score table, and type-based ZPM.

of x_{HO} slices would be significantly lower than 68% due to grouping slices into 1×4 vectors before compression, leading to low efficiency in the AQS-GEMM. To address this problem, the ZPM increases the number of compressible HO slices by adjusting the zero point during the PTQ's calibration as

$$z_p' = \begin{cases} 2^l \lfloor zp/2^l \rfloor + 2^{l-1}, & \text{if } zp > 0 \\ 0, & \text{otherwise,} \end{cases} \quad (7)$$

where l indicates the bit-width of LO slice, and z_p' indicates a manipulated zero-point. After adjusting the zero point, the frequent HO slice is also changed by $r' = (z_p' - 2^{l-1})_{HO}$. Note that *Panacea* uses $l = 4$ to divide an 8-bit value into two 4-bit slices. Fig. 8(b) shows the shifted distribution by the ZPM. The center of distribution (z_p') matches with the center of skip range, thereby putting more values in the skip range. The slice-level sparsity increases from 68% to 98%. The detailed slice-sparsity analysis on actual DNN benchmarks will be shown in Section IV. By increasing slice sparsity with the ZPM, the AQS-GEMM further reduces the number of operations by 33% for the FC layer of OPT-2.7B [60], compared to the AQS-GEMM without the ZPM. Note that we observed the slight distribution shift of the ZPM does not cause a considerable change in accuracy.

Distribution-based slicing. Although the ZPM successfully increases sparsity, the distribution of quantized values in some layers spreads over a wide range, resulting in low slice sparsity since fewer quantized values fall within the skip range. To enhance the slice sparsity of wide distributions, we newly propose DBS, which allows different slice's bit-widths depending on each activation distribution, enabling dynamic slice-skip ranges during inferences. During the calibration shown in Fig. 6, the DBS quantitatively analyzes the activation distribution for each layer and categorizes it into three types to determine the slice's bit-width. More precisely, the distribution monitoring step records histograms for quantized activations and then calculates their standard deviations (std). Then, as depicted in Fig. 9, ① Based on the std and z -score table,

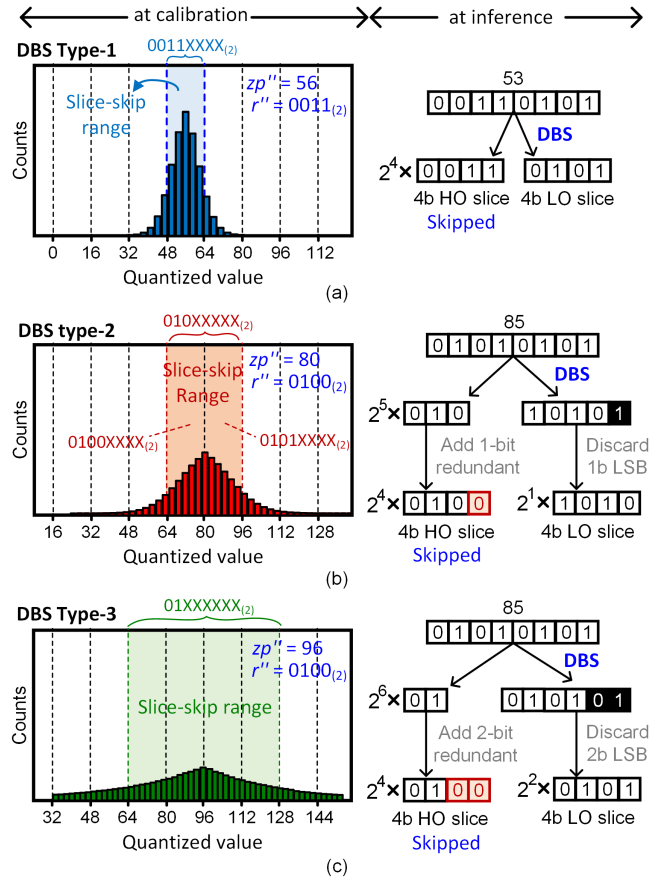


Fig. 10. Dynamically applying bit-slicing rules to different types during the inference phase: (a) DBS type-1, (b) DBS type-2, and (c) DBS type-3.

which contains the distribution's area from the mean up to a given $std \times z$, we categorize distributions into three types by comparing $std \times z$ to three distinct ranges. The DBS type-1 means the slice sparsity is originally high, and type-2 or 3 means the observed sparsity is lower than our target sparsity. To increase the slice sparsity for type-2 and type-3, the DBS allocates fewer bits to the HO slice and more bits to the LO slice ($l > 4$) than the basic scheme ($l = 4$). More precisely, we allocate $l = 4, 5,$ and 6 bits to the LO slice for type-1, type-2, and type-3, respectively, while we allocate $(8 - l)$ -bits to the HO slice for each type. This dynamic bit slicing will expand their slice-skip ranges to achieve our target sparsity at inference. ② Note that our calibration step employs a type-based ZPM by computing z_p'' and r'' based on the modified slice's bit-width l and (7) to maximize the slice sparsity.

In the inference step, given the identified DBS types and l , the DBS applies different slicing rules to compress and skip HO slices, as depicted in Fig. 10. For example, as shown in Fig. 10(b), type-2 divides the 8-bit integer $01010101_{(2)}$ into $010_{(2)}$ HO slice and $10101_{(2)}$ LO slice, thereby resulting in the effect of expanding the skip range by two times, thanks to observing more values in the range for $010_{(2)}$ HO slices compared to the range for $0101_{(2)}$. However, dynamically changing the slice bit width introduces significant hardware overhead. To prevent the issue, as depicted in Fig. 10, DBS maintains the

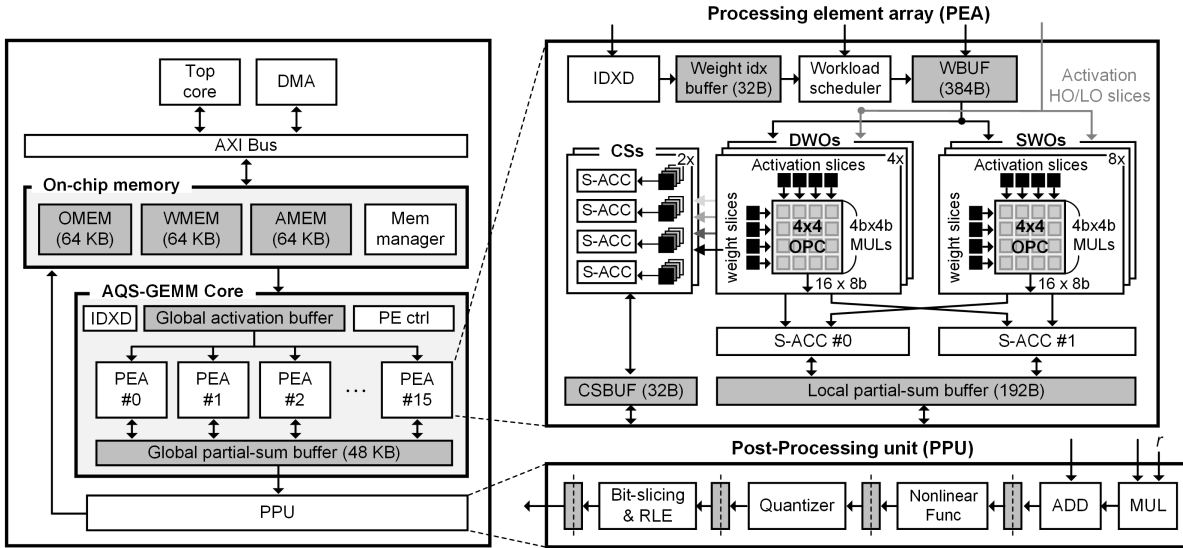


Fig. 11. Overall architecture of *Panacea* incorporating the AQS-GEMM core with 16 PEAs, each of which consists of 4 DWOs and 8 SWOs.

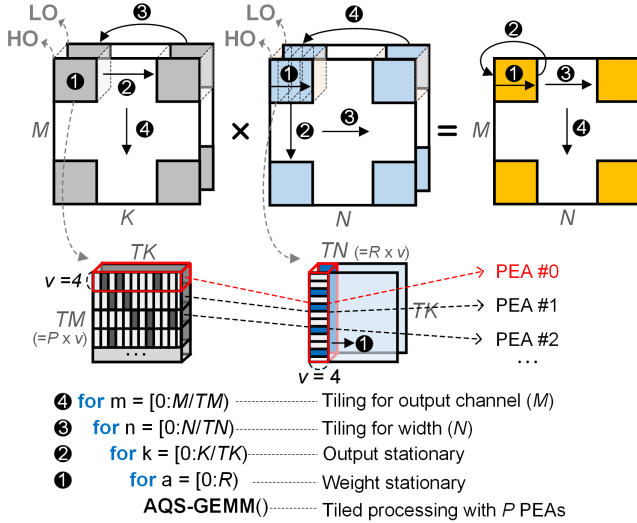


Fig. 12. *Panacea*'s output stationary dataflow computing the tiled AQS-GEMM to maximize data reuse.

4-bit width of slices by filling short HO slices with redundant zero bits and discarding LSBs in long LO slices. This increases the average slice sparsity by 20% (more than 50% for some layers) while causing an acceptable accuracy loss of 0.6%p on DeiT-base [3]. In terms of hardware, the DBS is simply implemented by properly shifting the outputs of AQS-GEMM, resulting in a small overhead. Consequently, the proposed DBS enables high slice sparsity in both narrow and wide distributions of activations, reducing EMA and maximizing the efficiency of AQS-GEMM in *Panacea*. The detailed evaluation results will be provided in Section IV.

D. Hardware Design

Overall architecture. Fig. 11 shows the overall architecture of *Panacea*, which consists of a top controller, on-chip memory, an AQS-GEMM core, and a post-processing unit (PPU). The on-chip memory is divided into weight memory (WMEM),

activation memory (AMEM), output memory (OMEM), and a memory manager. The AQS-GEMM core, with a global activation buffer and 16 processing element arrays (PEAs), efficiently computes the AQS-GEMM with weights and activations from the on-chip memory. Each PEA has an index decoder (IDX), a weight index buffer, a workload scheduler, a weight buffer (WBUF), dynamic workload operators (DWOs), static workload operators (SWOs), two compensators (CSs), a compensation buffer (CSBUF), a local partial-sum buffer and two shift-and-accumulator units (S-ACCs). With RLE indices, the IDX recovers the indices of uncompressed vectors and stores them in the weight index buffer. By matching the decoded weight indices with indices of activation vectors received from the global buffer, the workload scheduler allocates outer products for uncompressed slices into DWOs and SWOs. Each of DWO and SWO is comprised of an outer product calculator (OPC), which consists of 16 $4b \times 4b$ sign-unsigned multipliers to compute an outer product with a 4×1 weight slice-vector and a 1×4 activation slice-vector.

DWOs dynamically process $\mathbf{W}_{HO} \mathbf{x}_{HO}$, $\mathbf{W}_{LO} \mathbf{x}_{HO}$, and $\mathbf{W}_{HO} \mathbf{x}_{LO}$, while SWOs only handle the workload of dense operations, i.e., $\mathbf{W}_{LO} \mathbf{x}_{LO}$. Based on the current layer's DBS type, each S-ACCs properly shifts partial sums calculated by DWOs and SWOs, and accumulates them. Each CS consists of four small S-ACCs, which compute the compensation term of (6) by reusing the loaded weight slices. The PPU adds the bit-slice computation outputs and CSs outputs for exact GEMM calculations. After that, the PPU performs a non-linear function with the piecewise linear approximation, quantization, bit-slicing, HO slice compression, and RLE. The outputs of PPU, i.e., uncompressed slices, are stored in OMEM.

Dataflow. Fig.12 shows the dataflow of *Panacea* and its loop representation, illustrating how it manages data movement to enhance efficiency. *Panacea* supports an output stationary, eliminating the need for data movement of partial sums to ex-

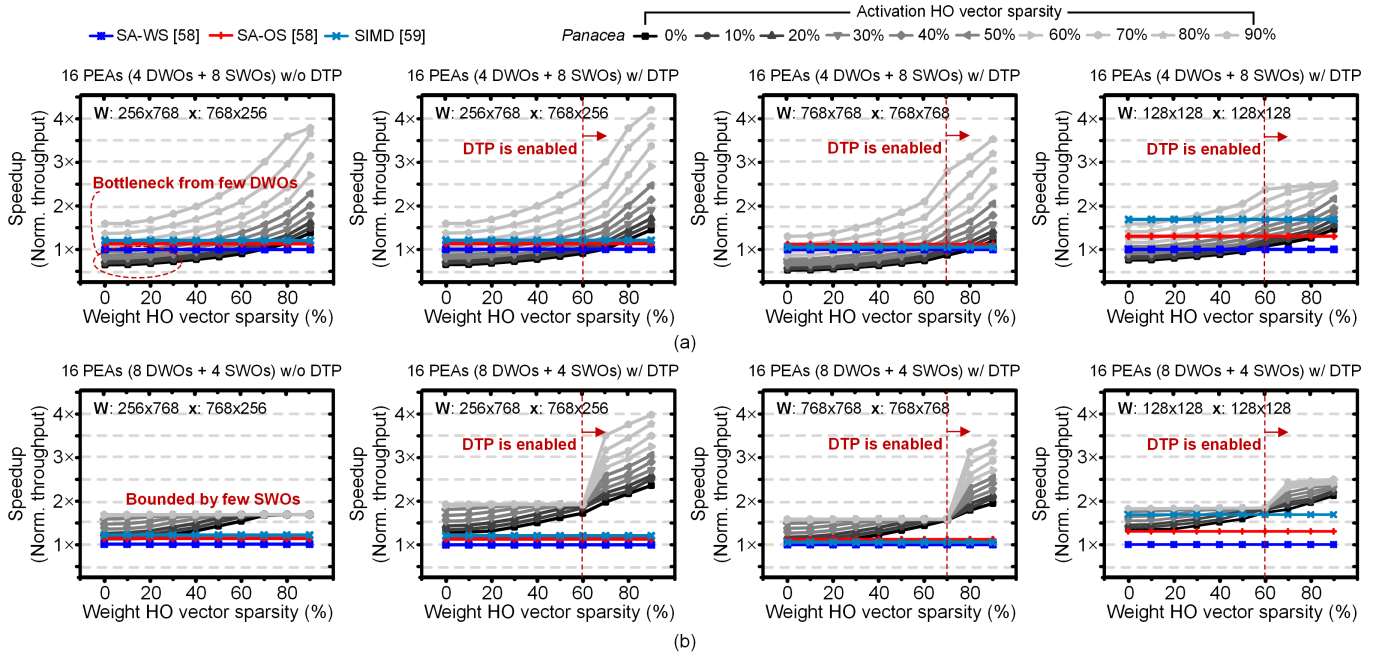


Fig. 13. Throughput evaluation of *Panacea* when using different design options, changing the HO slice sparsities of weight and activation, and changing the size of weight and activation; (a) 4 DWOs and 8 SWOs per PEA, and (b) 8 DWOs and 4 SWOs per PEA.

ternal memory. This dataflow significantly reduces the latency and energy consumption of accessing external memory. To maximize the reuse of weight, *Panacea* stores slices included in the $TM \times K$ weight tile into WMEM at once, if possible. *Panacea* computes the tiled AQS-GEMM, as depicted in Fig. 12. When the AQS-GEMM core processes a $TM \times TK$ weight tile along with a $TK \times TN$ activation tile, it assigns a $v \times TK$ weight sub-tile to each PEA, where each sub-tile includes both HO and LO slices, P indicates the number of PEAs, v indicates the length of slice vector, and $TM = Pv$. This allocation ensures that the workload is evenly distributed among the PEAs for efficient parallel processing. Furthermore, all PEAs share the $TK \times TN$ activation tile stored in the global activation buffer of the AQS-GEMM core, minimizing the repeated data load and removing the need for buffers storing the same activation tile. Each PEA reuses the $v \times TK$ weight sub-tile by R times, computing the tiled AQS-GEMM with HO and LO slices included in the $v \times TK$ weight sub-tile and $TK \times v$ activation sub-tile. The tiled AQS-GEMM successfully maximizes the data reuse of sub-tiles by allocating both HO sub-tiles (\mathbf{W}_{HO} and \mathbf{x}_{HO}) and LO sub-tiles (\mathbf{W}_{LO} and \mathbf{x}_{LO}) to a PEA and computing $\mathbf{W}_{HO}\mathbf{x}_{HO}$, $\mathbf{W}_{LO}\mathbf{x}_{HO}$, $\mathbf{W}_{HO}\mathbf{x}_{LO}$, and $\mathbf{W}_{LO}\mathbf{x}_{LO}$ in the PEA. This paper uses $v = 4$, $P = 16$, $TM = 64$, $TK = 32$, $TN = 64$, and $R = 16$.

Double tile processing. At a high HO slice sparsity, *Panacea* cannot fully utilize the space of on-chip memory and experiences low utilization of DWOs. To address the issue, we propose a double tile processing (DTP) that allows two different weight sub-tiles to be allocated into a PEA. The DTP is enabled if WMEM can store slices included in the $2TM \times K$ weight tile at once, and each PEA can store two

weight sub-tiles in its WBUF. When the DTP is enabled, each PEA seamlessly performs two-tiled processing for an activation sub-tile, maximizing the reuse of the activation sub-tile and increasing DWO's utilization. Under the DTP, the outer products of $\mathbf{W}_{LO}\mathbf{x}_{LO}$ for the second weight sub-tile can be allocated to DWOs to avoid the bounded throughput by few SWOs, as depicted in the first and second graphs of Fig. 13(b). The DTP allows each PEA to produce two 4×4 partial-sums at a time, thus each PEA needs two CSs, two S-ACCs, and the doubled local partial-sum buffer. Through the adoption of DTP, it is possible to achieve high utilization for both DWOs and SWOs, even at a high sparsity for weight HO slices. In addition, it significantly reduces data movement from external memory to *Panacea* and from AMEM to the AQS-GEMM core by increasing the data reuse of activation sub-tiles, improving the energy efficiency and throughput of *Panacea* without additional outer-product calculators.

IV. EVALUATION

Our evaluations demonstrate *Panacea*'s hardware efficiency, comparing it to the previous dense DNN accelerators including systolic array using weight stationary (SA-WS) and output stationary (SA-OS) [58], SIMD [59], and the recent bit-slice accelerator *Sibia* [53]. Note that SIMD, SA-WS, and SA-OS compute dense GEMM with 8-bit quantized weights and activations, while *Panacea* and *Sibia* use $4b \times 4b$ multipliers to compute bit-slice GEMMs. For a fair comparison, we make all designs to utilize identical design parameters: the number of multipliers, the size of on-chip SRAM, and the bandwidth between DRAM and accelerators. More precisely, we assume that they utilize 3072 $4b \times 4b$ multipliers, 256-bit/cycle DRAM bandwidth, 192KB on-chip SRAM to store

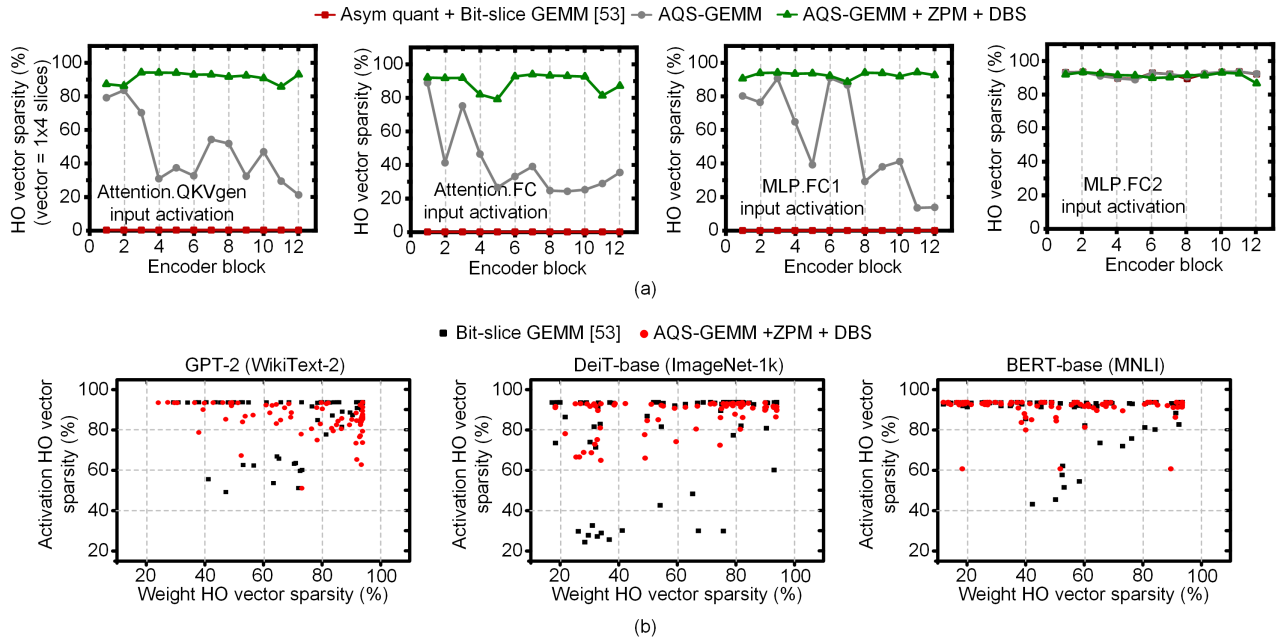


Fig. 14. (a) HO vector sparsity of activations in the DeiT-base model's layers (b) The vector sparsity of weight/activation HO slices observed by *Sibia* [53] and *Panacea* over all layers of the DNN benchmarks.

weights, input activations, and outputs, where an $8b \times 8b$ multiplier is equivalent to four $4b \times 4b$ multipliers. To estimate the energy cost of external memory, we use the DRAM emulator, CACTI 7.0 [79] and estimate the performance of designs based on a 28nm CMOS technology. Given a specific accelerator architecture and its data-flow, we count the number of cycles and the number of activated modules during inference based on Hugging-Face open-source DNN models, considering bit-slice sparsity in real benchmarks. Then, we use the obtained data to estimate energy with the post-layout results of building blocks like multipliers, adders, and buffers.

Throughput evaluation on different design options. Fig. 13 shows *Panacea*'s throughput improvement for different HO vector sparsities of weight/activation, compared to the previous accelerators [58], [59]. Fig. 13(a) and (b) present scenarios with 16 PEAs, each having different numbers of DWOs and SWOs. The graphs also illustrate the effect of DTP and different weight/activation sizes. More precisely, Fig. 13(a) shows throughput in the case of using 4 DWOs and 8 SWOs per PEA. In situations where the HO slice sparsity of weight and activation is low, *Panacea* achieves lower throughput than the previous designs [58], [59]. This is because $\mathbf{W}_{HO} \mathbf{x}_{HO}, \mathbf{W}_{LO} \mathbf{x}_{HO}, \mathbf{W}_{HO} \mathbf{x}_{LO}$ become dense bit-slice GEMMs, and they are allocated to few DWOs, resulting in a long delay from DWOs. Conversely, at the high slice sparsity, *Panacea* achieves up to $3.7\times$, $3.35\times$, and $3.14\times$ speedup when compared to SA-WS, SA-OS [58], and SIMD [59], respectively. By applying the proposed DTP at high sparsity scenarios, *Panacea*'s throughput is further improved by $1.11\times$ than the disabled DTP mode. Fig. 13(b) shows the throughput of *Panacea* using 8 DWOs and 4 SWOs in each PEA. Although the throughput is still lower than SIMD [59] design at very low sparsity, the use of more DWOs has

narrowed the gap in dense conditions. When the vector sparsity increases, the limited number of SWOs bounds the speedup. In such cases, *Panacea* provides higher throughput by adopting the proposed DTP. However, as the size of weight increases, as illustrated in Fig. 13(b), the DTP starts to be enabled at higher vector sparsity due to the difficulty of meeting the DTP enable condition. Compared to previous DNN accelerators [57]–[59], *Panacea* achieves better speedup with large-sized weights and activations, significantly reducing off-/on-chip memory accesses due to its data-compression. In the case of a small-sized activation, as shown in Fig. 13, all DNN accelerators can store the entire activation at once. This easily avoids repeated data access and consequently reduces the effectiveness of data movement based on compression. Ultimately, an appropriate number of DWOs and SWOs can be determined by analyzing slice-vector sparsity in actual DNNs, as depicted in Fig. 14.

Vector-level sparsity evaluation on DNN benchmarks. Since the AQS-GEMM applies compression at the vector level, as shown in Fig. 7, it is crucial to examine the sparsity at the vector level. Fig. 14(a) shows the HO vector sparsity of asymmetrically quantized activations in different GEMM methods, especially for DeiT-base [3]. The previous bit-slice GEMMs [53], [54] cannot utilize any vector sparsity for most of the layers due to asymmetric quantization, which produces nonzero slices that cannot be skipped. Note that a non-linear function in MLP produces many near-zero values that result in a lot of zero HO slices even with asymmetric quantization, so the previous bit-slice GEMM only achieves high vector sparsity in the activation of MLP.FC2 layer, as shown in Fig. 14(a). In contrast, the AQS-GEMM enables the vector sparsity for all layers by compressing frequent HO slices at the vector level. The ZPM and DBS further increase the vector sparsity for wide distributions.

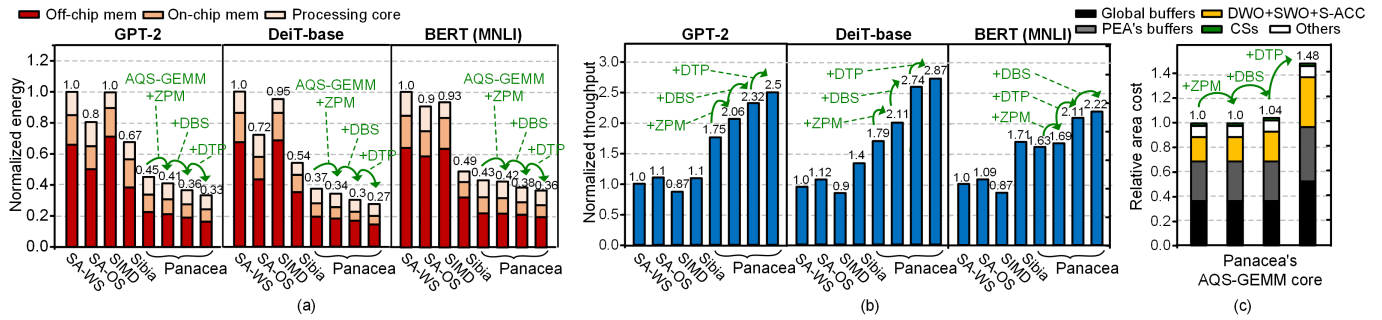


Fig. 15. (a) Energy breakdown and (b) throughput of the DNN accelerators for different benchmarks. (c) Relative area cost for applying the proposed methods. Note that we assume that all designs use identical hardware resources, such as the size of on-chip memory and the number of multipliers.

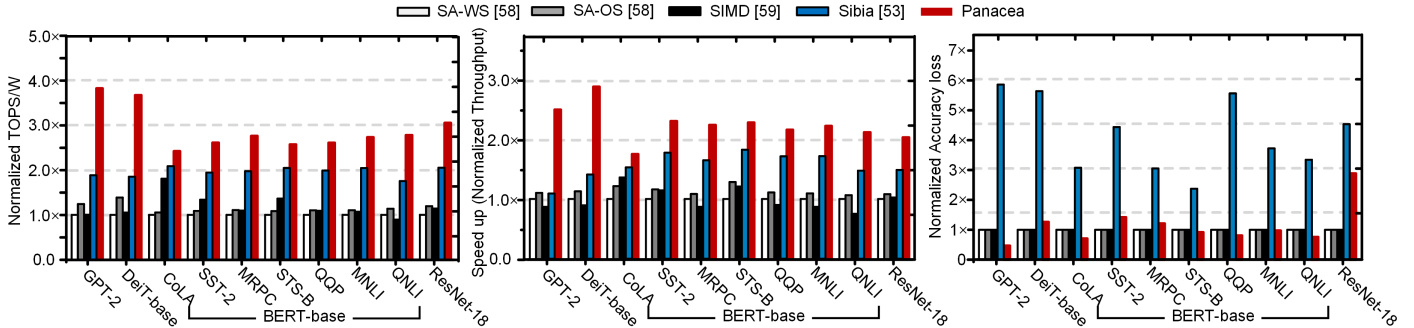


Fig. 16. Energy efficiency, throughput, and accuracy loss evaluations of *Panacea* and previous accelerators [53], [58], [59] on different DNN models. Note that we assume that all designs use 192KB on-chip memory and 3072 $4b \times 4b$ multipliers, where an $8b \times 8b$ multiplier is identical to four $4b \times 4b$ multipliers.

Fig. 14(b) presents comparisons between the AQS-GEMM of *Panacea* and the bit-slice GEMM of *Sibia* [53] in terms of the weight/activation HO vector sparsity across all layers within three transformer models: DeiT-base [3], BERT-base [5], and GPT-2 [7]¹. Two methods utilize the identical SBR for the weight’s bit-slicing, thus they achieve the same HO vector sparsity for weights. While the bit-slice GEMM [53] achieves high HO vector sparsity in activations with symmetric quantization, the AQS-GEMM also achieves comparable vector sparsity with asymmetric quantization. In several layers, the AQS-GEMM outperforms the bit-slice GEMM [53] by increasing HO vector sparsity through the ZPM and DBS.

Performance breakdown and trade-off analysis. To evaluate large-scale DNN benchmarks, *Panacea* is designed with 4 DWOs and 8 SWOs in each PEA, as shown in Fig. 13, providing consistently high throughput across various levels of vector sparsity in weights. This configuration is based on observations from Fig. 14(b), where most activations have very high vector sparsity while weights have varying vector sparsity. Furthermore, given the large size of weights and activations in transformer models, using fewer DWOs successfully improves performance. Fig. 15 shows the energy breakdown and the trade-off between energy, throughput, and area-overhead. By handling only uncompressed slices within the AQS-GEMM, *Panacea* significantly reduces the number of off/on-chip mem-

ory accesses and improves hardware-efficiency, compared to previous designs [53], [58], [59]. *Panacea*’s performance is further enhanced by gradually adopting the proposed the ZPM, DBS, and DTP. For GPT-2 [7] and the WikiText-2 [80], the ZPM further improves energy consumption by 10% and throughput by 17%, increasing slice-level sparsity without any area overhead. The DBS also improves energy consumption by 11% and throughput by 12%, requiring small area overhead due to its additional shifting units in the AQS-GEMM core. By enhancing hardware utilization for high slice-vector sparsity in DNN layers, the DTP reduces energy consumption by 8.9% and improves throughput by 7.6%. However, it requires additional buffers and larger on-chip memory, resulting in some area overhead.

Accelerator performance for DNN models. Fig. 16 presents results for the various large transformer-based models [3], [5], [7] and a small non-transformer-based model [1]. In specific, for GPT-2 [7] and the WikiText-2 dataset [80] including large-sized activations, *Panacea* achieves $3.82\times$, $3.07\times$, $3.81\times$, and $2.03\times$ higher energy efficiency (TOPS/W) than SA-WS, SA-OS [57], [58], SIMD [59], and *Sibia* [53], respectively, successfully achieving high activation sparsity based on the proposed ZPM and DBS. For BERT-base [5] and the GLUE [75] dataset, which uses fewer tokens, *Panacea* still outperforms the dense DNN accelerators [58], [59] by achieving $2.67\times$ and $2.41\times$ higher energy efficiency in average, respectively, due to the compressed data movement from external memory to the AQS-GEMM core.

¹Bit-slice GEMMs adopt 10-bit symmetric weight quantization in MLP layers of GPT-2 [7] to avoid accuracy loss, segmenting a 10-bit integer into three slices based on SBR.

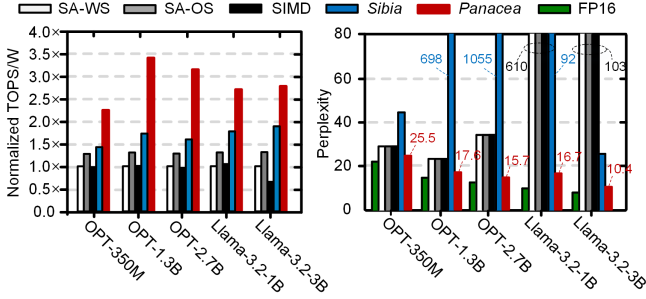


Fig. 17. Energy efficiency and perplexity evaluations of *Panacea* and previous DNN accelerators [53], [58], [59] on different LLMs.

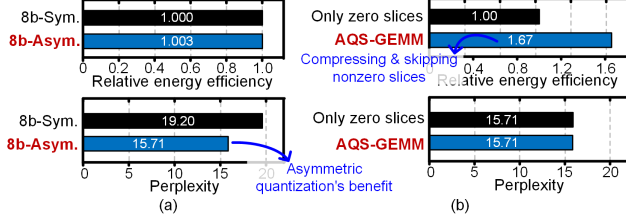


Fig. 18. Relative energy efficiency and perplexity for OPT-2.7B [60] when (a) using different quantization methods in *Panacea* and (b) using the same asymmetric quantization in two versions of *Panacea*.

Fig. 17 presents the evaluation results for various large language models (LLMs) [60], [61] using the WikiText-2 dataset [80]. *Panacea* achieves 1.57 \times , 1.97 \times , and 1.96 \times higher energy efficiency compared to *Sibia* in the OPT models [60] with 350M, 1.3B, and 2.7B parameters, respectively, while maintaining perplexity (PPL) similar to FP16. Unlike the OPT models [60], the Llama-3.2 models [61] are more challenging to quantize weights without PPL loss due to structural differences and large outliers. To address these challenges, we applied OPTQ [46], a weight-only quantization, and 64 channel-wise quantization to weights. Especially in the case of *Sibia* [53] and *Panacea*, which support mixed-precision quantization, the inputs to sensitivity-critical layers, i.e., the down-projection layer, can be expressed with three bit-slices, resulting in better PPL than dense GEMM architectures [58], [59]. For the Llama-3.2 3B model, *Panacea* achieves 2.77 \times , 2.11 \times , 4.24 \times , and 1.47 \times greater energy efficiency compared to the SA-WS, the SA-OS [58], the SIMD [59], and *Sibia* [53], respectively, even when considering mixed-precision quantization.

Decoupling the advantages of asymmetric quantization and the AQS-GEMM. *Panacea* supports not only asymmetric quantization for activations, but also symmetric quantization by setting every zero-point to 128 within the 8-bit range. Fig. 18(a) compares the two quantization methods on *Panacea* for OPT-2.7B [60] and shows that while asymmetric quantization yields a lower PPL, the energy efficiency and the throughput remain nearly equivalent due to the ZPM and DBS maximizing the slice sparsity. Additionally, Fig. 18(b) demonstrates that *Panacea*, utilizing the AQS-GEMM to skip both nonzero and zero slices, improves energy efficiency by 1.67 \times and throughput by 2.10 \times compared to skipping only zero slices,

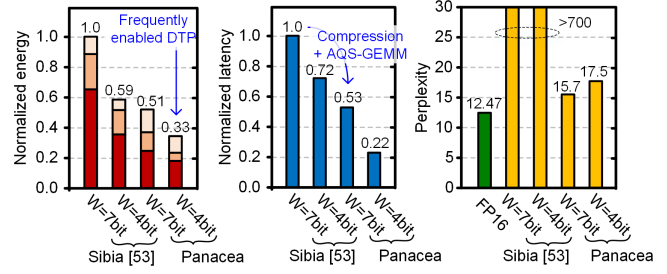
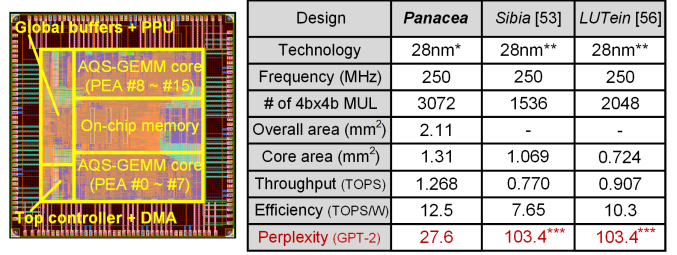


Fig. 19. Energy breakdown, latency, and perplexity of *Sibia* [53] and *Panacea* when they use 4-bit or 7-bit weights for OPT-2.7B [46], [60].



*FD-SOI technology **CMOS technology ***7-bit sym.quantization for all activations

Fig. 20. The layout of *Panacea* and ASIC-level comparison table.

while both achieve the same PPL by producing exact results in the AQS-GEMM.

Accelerator performance in low-bit quantization. As mentioned in Section III-B, *Panacea* divides a $(3n+4)$ -bit weight into $(n+1)$ 4-bit slices and a $(4k+4)$ -bit activation into $(k+1)$ 4-bit slices. Note that *Sibia* [53] uses symmetrically quantized activations, limiting its representation to $(3k+4)$ bits, despite using $(k+1)$ 4-bit slices. Fig. 19 compares the performance of *Sibia* [53] and *Panacea*, on OPT-2.7B for $n=0$ or $n=1$ with $k=1$. The 4-bit quantization for weights ($n=0$) was handled with OPTQ [46], which prevents PPL loss in extreme-low-bit quantization (≤ 4 -bit). *Panacea* consumes only 56% of energy compared to *Sibia* [53] as the DTP is frequently enabled due to the 4-bit weights without HO slices. *Panacea* further outperforms *Sibia* [53] by achieving 1.9 \times and 3.3 \times lower latency for 7-bit and 4-bit weights, respectively, while still maintaining the acceptable PPL.

ASIC implementation. *Panacea* is implemented in a 28nm FD-SOI technology. Fig. 20 shows its layout and a comparison table summarizing implementation results of the recent bit-slice DNN accelerators: *Sibia* [53], *LUTein* [56], and *Panacea*. To support the proposed methods and 2 \times more multipliers, *Panacea* requires a small overhead in terms of the core area. Due to supporting the proposed AQS-GEMM and sparsity optimization methods, *Panacea* simultaneously achieves better throughput, energy efficiency, and algorithm-level performance on large-scale DNN models.

V. CONCLUSION

This paper proposes a bit-slice DNN accelerator, *Panacea*, that enables the bit-slice GEMM with asymmetric quantization. *Panacea*'s AQS-GEMM compresses high-order slices

frequently observed in asymmetric quantization and skips their computations. To improve the efficiency of AQS-GEMM, *Panacea* presents two algorithm-hardware co-optimization methods: ZPM and DBS, which increase slice-vector sparsity for activations. To efficiently support the proposed methods, each processing element of *Panacea* dedicates two types of operators and utilizes the specialized dataflow, maximizing data reuse. Consequently, *Panacea* provides attractive hardware/algorithm performances during DNN inferences. Our DNN evaluation code will be open-sourced at <https://github.com/Dongyunkam/Panacea>.

VI. ACKNOWLEDGMENTS

We express our gratitude to the anonymous reviewers for their valuable comments and insightful suggestions. This work was supported in part by Korea Institute for Advancement of Technology (KIAT) grant funded by the Korea Government (MOTIE) (P0017304, Human Resource Development Program for Industrial Innovation), in part by the National Research Foundation of Korea (NRF) grant funded by the Korea government (MSIT) (No. 2022R1A2C2092521), in part by the NAVER-Intel Co-Lab, and in part by the IC Design Education Center (IDEC).

REFERENCES

- [1] Kaiming He, Xiangyu Zhang, Shaoqing Ren, and Jian Sun. Deep residual learning for image recognition. In *Proc. IEEE Conference on Computer Vision and Pattern Recognition (CVPR)*, pages 770–778, 2016.
- [2] Alexey Dosovitskiy, Lucas Beyer, Alexander Kolesnikov, Dirk Weissenborn, Xiaohua Zhai, Thomas Unterthiner, Mostafa Dehghani, Matthias Minderer, Georg Heigold, Sylvain Gelly, Jakob Uszkoreit, and Neil Houlsby. An image is worth 16x16 words: Transformers for image recognition at scale. In *arXiv.org*, 2020.
- [3] Hugo Touvron, Matthieu Cord, Matthijs Douze, Francisco Massa, Alexandre Sablayrolles, and Hervé Jégou. Training data-efficient image transformers & distillation through attention. In *Proc. International conference on machine learning (ICML)*, pages 10347–10357, 2021.
- [4] Shuohang Wang and Jing Jiang. Learning natural language inference with LSTM. In *arXiv.org*, 2015.
- [5] Jacob Devlin, Ming-Wei Chang, Kenton Lee, and Kristina Toutanova. Bert: Pre-training of deep bidirectional transformers for language understanding. In *arXiv.org*, 2018.
- [6] Alec Radford, Karthik Narasimhan, Tim Salimans, and Ilya Sutskever. Improving language understanding by generative pre-training, 2018.
- [7] Alec Radford, Jeffrey Wu, Rewon Child, David Luan, Dario Amodei, and Ilya Sutskever. Language models are unsupervised multitask learners. *OpenAI blog*, 1(8):9, 2019.
- [8] Luciano Floridi and Massimo Chiriatti. GPT-3: Its nature, scope, limits, and consequences. *Minds Mach.*, 30:681–694, 2020.
- [9] Hugo Touvron, Louis Martin, Kevin Stone, Peter Albert, Amjad Almahairi, Yasmine Babaei, Nikolay Bashlykov, Soumya Batra, Prajjwal Bhargava, Shrutit Bhosale, Dan Bikel, Lukas Blecher, Cristian Canton Ferrer, Moya Chen, Guillem Cucurull, David Esiobu, Jude Fernandes, Jeremy Fu, Wenyin Fu, Brian Fuller, Cynthia Gao, Vedanuj Goswami, Naman Goyal, Anthony Hartshorn, Saghar Hosseini, Rui Hou, Hakan Inan, Marcin Kardas, Viktor Kerkez, Madian Khabsa, Isabel Kloumann, Artem Korenev, Punit Singh Koura, Marie-Anne Lachaux, Thibaut Lavril, Jenya Lee, Diana Liskovich, Yinghai Lu, Yuning Mao, Xavier Martinet, Todor Mihaylov, Pushkar Mishra, Igor Molybog, Yixin Nie, Andrew Poulton, Jeremy Reizenstein, Rashi Rungta, Kalyan Saladi, Alan Schelten, Ruan Silva, Eric Michael Smith, Ranjan Subramanian, Xiaoqing Ellen Tan, Binh Tang, Ross Taylor, Adina Williams, Jian Xiang Kuan, Puxin Xu, Zheng Yan, Iliyan Zarov, Yuchen Zhang, Angela Fan, Melanie Kambadur, Sharan Narang, Aurolien Rodriguez, Robert Stojnic, Sergey Edunov, and Thomas Scialom. Llama 2: Open foundation and fine-tuned chat models. 2023.
- [10] Zhi Zhou, Xu Chen, En Li, Liekang Zeng, Ke Luo, and Junshan Zhang. Edge intelligence: Paving the last mile of artificial intelligence with edge computing. *Proc. IEEE*, 107(8):1738–1762, 2019.
- [11] Kyeong-Beom Park, Minseok Kim, Sung Ho Choi, and Jae Yeol Lee. Deep learning-based smart task assistance in wearable augmented reality. *Robot. Comput.-Integr. Manuf.*, 63:101887, 2020.
- [12] Girish Sastry, Lennart Heim, Haydn Belfield, Markus Anderljung, Miles Brundage, Julian Hazell, Cullen O’Keefe, Gillian K Hadfield, Richard Ngo, Konstantin Pilz, Geroge Gor, Emma Bluemke, Sarah Shoker, Janet Egan, Robert F. Trager, Shahar Avin, Adrian Weller, Yoshua Bengio, and Diane Coyle. Computing Power and the Governance of Artificial Intelligence. In *arXiv.org*, 2024.
- [13] Jared Kaplan, Sam McCandlish, Tom Henighan, Tom B Brown, Benjamin Chess, Rewon Child, Scott Gray, Alec Radford, Jeffrey Wu, and Dario Amodei. Scaling laws for neural language models. In *arXiv.org*, 2020.
- [14] Qingqing Cao, Aruna Balasubramanian, and Niranjan Balasubramanian. Towards accurate and reliable energy measurement of NLP models, 2020.
- [15] Sehoon Kim, Coleman Hooper, Thanakul Wattanawong, Minwoo Kang, Ruohan Yan, Hasan Genc, Grace Dinh, Qijing Huang, Kurt Keutzer, Michael W Mahoney, Yakun Sophia Shao, and Amir Gholami. Full stack optimization of transformer inference: a survey, 2023.
- [16] Yingchun Wang, Jingyi Wang, Weizhan Zhang, Yufeng Zhan, Song Guo, Qinghua Zheng, and Xuanyu Wang. A survey on deploying mobile deep learning applications: A systemic and technical perspective. *Digit. Commun. Netw.*, 8(1):1–17, 2022.
- [17] Hanan Hussain, PS Tamizharasan, and CS Rahul. Design possibilities and challenges of DNN models: a review on the perspective of end devices. *Artif. Intell. Rev.*, pages 1–59, 2022.
- [18] Di Wu, Qi Tang, Yongle Zhao, Ming Zhang, Ying Fu, and Debing Zhang. Easyquant: Post-training quantization via scale optimization. In *arXiv.org*, 2020.
- [19] Zhenhua Liu, Yunhe Wang, Kai Han, Wei Zhang, Siwei Ma, and Wen Gao. Post-training quantization for vision transformer. In *Proc. Advances in neural information processing systems (NeurIPS)*, volume 34, pages 28092–28103, 2021.
- [20] Yuhang Li, Ruihao Gong, Xu Tan, Yang Yang, Peng Hu, Qi Zhang, Fengwei Yu, Wei Wang, and Shi Gu. Brecq: Pushing the limit of post-training quantization by block reconstruction. In *arXiv.org*, 2021.
- [21] Ron Banner, Yury Nahshan, Elad Hoffer, and Daniel Soudry. Acq: Analytical clipping for integer quantization of neural networks. In *arXiv.org*, 2018.
- [22] Guangxuan Xiao, Ji Lin, Mickael Seznec, Hao Wu, Julien Demouth, and Song Han. Smoothquant: Accurate and efficient post-training quantization for large language models. In *Proc. International conference on machine learning (ICML)*, pages 38087–38099, 2023.
- [23] Yang Lin, Tianyu Zhang, Peiqin Sun, Zheng Li, and Shuchang Zhou. Fq-vit: Post-training quantization for fully quantized vision transformer. In *arXiv.org*, 2021.
- [24] Jiawei Liu, Lin Niu, Zhihang Yuan, Dawei Yang, Xinggong Wang, and Wenyu Liu. Pd-quant: Post-training quantization based on prediction difference metric. In *Proc. IEEE Conference on Computer Vision and Pattern Recognition (CVPR)*, pages 24427–24437, 2023.
- [25] Jung Hyun Lee, Jeonghoon Kim, Se Jung Kwon, and Dongsu Lee. Flexround: Learnable rounding based on element-wise division for post-training quantization. In *Proc. International conference on machine learning (ICML)*, pages 18913–18939, 2023.
- [26] Yaohui Cai, Zhewei Yao, Zhen Dong, Amir Gholami, Michael W Mahoney, and Kurt Keutzer. Zeroq: A novel zero shot quantization framework. In *Proc. IEEE Conference on Computer Vision and Pattern Recognition (CVPR)*, pages 13169–13178, 2020.
- [27] Zhikai Li, Junrui Xiao, Lianwei Yang, and Qingyi Gu. Repq-vit: Scale reparameterization for post-training quantization of vision transformers. In *Proc. International Conference on Computer Vision (ICCV)*, pages 17227–17236, 2023.
- [28] Xiuying Wei, Yunchen Zhang, Xiangguo Zhang, Ruihao Gong, Shanghang Zhang, Qi Zhang, Fengwei Yu, and Xianglong Liu. Outlier suppression: Pushing the limit of low-bit transformer language models. In *Proc. Advances in neural information processing systems (NeurIPS)*, volume 35, pages 17402–17414, 2022.
- [29] Xiuying Wei, Yunchen Zhang, Yuhang Li, Xiangguo Zhang, Ruihao Gong, Jinyang Guo, and Xianglong Liu. Outlier suppression+: Accurate

- quantization of large language models by equivalent and optimal shifting and scaling. In *arXiv.org*, 2023.
- [30] Markus Nagel, Marios Fournarakis, Rana Ali Amjad, Yelysei Bondarenko, Mart Van Baalen, and Tijmen Blankevoort. A white paper on neural network quantization. In *arXiv.org*, 2021.
- [31] Jing Liu, Ruihao Gong, Xiuying Wei, Zhiwei Dong, Jianfei Cai, and Bohan Zhuang. Qllm: Accurate and efficient low-bitwidth quantization for large language models. In *arXiv.org*, 2023.
- [32] Wenqi Shao, Mengzhao Chen, Zhaoyang Zhang, Peng Xu, Lirui Zhao, Zhiqian Li, Kaipeng Zhang, Peng Gao, Yu Qiao, and Ping Luo. Omniquant: Omnidirectionally calibrated quantization for large language models. In *arXiv.org*, 2023.
- [33] Man Shi, Vikram Jain, Antony Joseph, Maurice Meijer, and Marian Verhelst. Bitwave: Exploiting column-based bit-level sparsity for deep learning acceleration. In *Proc. the International Symposium on High-Performance Computer Architecture (HPCA)*, pages 732–746, 2024.
- [34] Shijin Zhang, Zidong Du, Lei Zhang, Huiying Lan, Shaoli Liu, Ling Li, Qi Guo, Tianshi Chen, and Yunji Chen. Cambricon-X: An accelerator for sparse neural networks. In *Proc. International Symposium on Microarchitecture (MICRO)*, pages 1–12, 2016.
- [35] Maohua Zhu, Tao Zhang, Zhenyu Gu, and Yuan Xie. Sparse tensor core: Algorithm and hardware co-design for vector-wise sparse neural networks on modern gpus. In *Proc. International Symposium on Microarchitecture (MICRO)*, pages 359–371, 2019.
- [36] Song Han, Jeff Pool, John Tran, and William Dally. Learning both weights and connections for efficient neural network. In *Proc. Advances in neural information processing systems (NeurIPS)*, volume 28, 2015.
- [37] Chao Fang, Aojun Zhou, and Zhongfeng Wang. An algorithm–hardware co-optimized framework for accelerating n: M sparse transformers. *IEEE Trans. Very Large Scale Integr. (VLSI) Syst.*, 30(11):1573–1586, 2022.
- [38] Jung Gyu Min, Dongyun Kam, Younghoon Byun, Gunho Park, and Youngjoo Lee. Energy-efficient risc-v-based vector processor for cache-aware structurally-pruned transformers. In *Proc. IEEE/ACM International Symposium on Low Power Electronics and Design (ISLPED)*, pages 1–6, 2023.
- [39] Younghoon Byun, Seungsik Moon, Baeseong Park, Se Jung Kwon, Dongsoo Lee, Gunho Park, Eunji Yoo, Jung Gyu Min, and Youngjoo Lee. Sparsity-Aware Memory Interface Architecture using Stacked XORNet Compression for Accelerating Pruned-DNN Models. *Proc. Machine Learning and Systems (MLSys)*, 5, 2023.
- [40] Elias Frantar and Dan Alistarh. Sparsegpt: Massive language models can be accurately pruned in one-shot. In *Proc. International conference on machine learning (ICML)*, pages 10323–10337, 2023.
- [41] Sehoon Kim, Amir Gholami, Zhewei Yao, Michael W Mahoney, and Kurt Keutzer. I-bert: Integer-only bert quantization. In *Proc. International conference on machine learning (ICML)*, pages 5506–5518, 2021.
- [42] Benoit Jacob, Skirmantas Kligys, Bo Chen, Menglong Zhu, Matthew Tang, Andrew Howard, Hartwig Adam, and Dmitry Kalenichenko. Quantization and training of neural networks for efficient integer-arithmetic-only inference. In *Proc. IEEE Conference on Computer Vision and Pattern Recognition (CVPR)*, pages 2704–2713, 2018.
- [43] Cong Guo, Jiaming Tang, Weiming Hu, Jingwen Leng, Chen Zhang, Fan Yang, Yunxin Liu, Minyi Guo, and Yuhao Zhu. Olive: Accelerating large language models via hardware-friendly outlier-victim pair quantization. In *Proc. International Symposium on Computer Architecture (ISCA)*, pages 1–15, 2023.
- [44] Steve Dai, Rangha Venkatesan, Mark Ren, Brian Zimmer, William Dally, and Brucek Khailany. Vs-quant: Per-vector scaled quantization for accurate low-precision neural network inference. In *Proc. Machine Learning and Systems (MLSys)*, volume 3, pages 873–884, 2021.
- [45] Ali Hadi Zadeh, Isak Edo, Omar Mohamed Awad, and Andreas Moshovos. Gobo: Quantizing attention-based nlp models for low latency and energy efficient inference. In *Proc. International Symposium on Microarchitecture (MICRO)*, pages 811–824, 2020.
- [46] Elias Frantar, Saleh Ashkboos, Torsten Hoefler, and Dan Alistarh. OPTQ: Accurate quantization for generative pre-trained transformers. In *Proc. International Conference on Learning Representations (ICLR)*, 2022.
- [47] Zhihang Yuan, Lin Niu, Jiawei Liu, Wenyu Liu, Xinggong Wang, Yuzhang Shang, Guangyu Sun, Qiang Wu, Jiayang Wu, and Bingzhe Wu. Rptq: Reorder-based post-training quantization for large language models. In *arXiv.org*, 2023.
- [48] Cong Guo, Chen Zhang, Jingwen Leng, Zihan Liu, Fan Yang, Yunxin Liu, Minyi Guo, and Yuhao Zhu. Ant: Exploiting adaptive numerical data type for low-bit deep neural network quantization. In *Proc. International Symposium on Microarchitecture (MICRO)*, pages 1414–1433, 2022.
- [49] Shuchang Zhou, Yuxin Wu, Zekun Ni, Xinyu Zhou, He Wen, and Yuheng Zou. Dorefa-net: Training low bitwidth convolutional neural networks with low bitwidth gradients. In *arXiv.org*, 2016.
- [50] Yijiang Liu, Huanrui Yang, Zhen Dong, Kurt Keutzer, Li Du, and Shanghang Zhang. Noisyquant: Noisy bias-enhanced post-training activation quantization for vision transformers. In *Proc. IEEE Conference on Computer Vision and Pattern Recognition (CVPR)*, pages 20321–20330, 2023.
- [51] Zhihang Yuan, Chenhao Xue, Yiqi Chen, Qiang Wu, and Guangyu Sun. Ptq4vit: Post-training quantization for vision transformers with twin uniform quantization. In *Proc. the European conference on computer vision (ECCV)*, pages 191–207, 2022.
- [52] Yujun Lin, Haotian Tang, Shang Yang, Zhekai Zhang, Guangxuan Xiao, Chuang Gan, and Song Han. Qserve: W4a8kv4 quantization and system co-design for efficient llm serving. 2024.
- [53] Dongseok Im, Gwangtae Park, Zhiyong Li, Junha Ryu, and Hoi-Jun Yoo. Sibia: Signed bit-slice architecture for dense dnn acceleration with slice-level sparsity exploitation. In *Proc. the International Symposium on High-Performance Computer Architecture (HPCA)*, pages 69–80, 2023.
- [54] Gil Shomron and Uri Weiser. Non-blocking simultaneous multithreading: Embracing the resiliency of deep neural networks. In *Proc. International Symposium on Microarchitecture (MICRO)*, pages 256–269, 2020.
- [55] Donghyeon Han and Hoi-Jun Yoo. Hnpu-v1: An adaptive dnn training processor utilizing stochastic dynamic fixed-point and active bit-precision searching. In *On-Chip Training NPU-Algorithm, Architecture and SoC Design*, pages 121–161. Springer, 2023.
- [56] Dongseok Im and Hoi-Jun Yoo. Lutein: Dense-sparse bit-slice architecture with radix-4 lut-based slice-tensor processing units. In *Proc. the International Symposium on High-Performance Computer Architecture (HPCA)*, pages 747–759, 2024.
- [57] Marian Verhelst and Bert Moons. Embedded deep neural network processing: Algorithmic and processor techniques bring deep learning to iot and edge devices. *IEEE Solid-State Circuits Mag.*, 9(4):55–65, 2017.
- [58] Bahar Asgari, Ramyad Hadidi, and Hyesoon Kim. MEISSA: Multiplying matrices efficiently in a scalable systolic architecture. In *Proc. International Conference on Computer Design (ICCD)*, pages 130–137, 2020.
- [59] Ben Keller, Rangharajan Venkatesan, Steve Dai, Stephen G Tell, Brian Zimmer, Charbel Sakr, William J Dally, C Thomas Gray, and Brucek Khailany. A 95.6-TOPS/W deep learning inference accelerator with per-vector scaled 4-bit quantization in 5 nm. *IEEE J. Solid-State Circuits*, 58(4):1129–1141, 2023.
- [60] Susan Zhang, Stephen Roller, Naman Goyal, Mikel Artetxe, Moya Chen, Shuohui Chen, Christopher Dewan, Mona Diab, Xian Li, Xi Victoria Lin, Todor Mihaylov, Myle Ott, Sam Shleifer, Kurt Shuster, Daniel Simig, Punit Singh Koura, Anjali Sridhar, Tianlu Wang, and Luke Zettlemoyer. Opt: Open pre-trained transformer language models. 2022.
- [61] Meta AI. Llama 3.2: Revolutionizing edge ai and vision with open, customizable models. <https://ai.meta.com/blog/llama-3-2-connect-2024-vision-edge-mobile-devices>, 2024.
- [62] Xiaoxia Wu, Zhewei Yao, Minjia Zhang, Conglong Li, and Yuxiong He. Xtc: Extreme compression for pre-trained transformers made simple and efficient. In *Proc. Advances in neural information processing systems (NeurIPS)*, volume 35, pages 3217–3231, 2022.
- [63] Eunhyeok Park, Dongyoung Kim, and Sungjoo Yoo. Energy-efficient neural network accelerator based on outlier-aware low-precision computation. In *Proc. International Symposium on Computer Architecture (ISCA)*, pages 688–698, 2018.
- [64] Zhuoran Song, Bangqi Fu, Feiyang Wu, Zhaoming Jiang, Li Jiang, Naifeng Jing, and Xiaoyao Liang. Drq: dynamic region-based quantization for deep neural network acceleration. In *Proc. International Symposium on Computer Architecture (ISCA)*, pages 1010–1021, 2020.
- [65] Jaeyong Jang, Yulhwa Kim, Juheun Lee, and Jae-Joon Kim. FIGNA: Integer Unit-Based Accelerator Design for FP-INT GEMM Preserving Numerical Accuracy. In *Proc. the International Symposium on High-Performance Computer Architecture (HPCA)*, pages 760–773, 2024.
- [66] Yury Nahshan, Brian Chmiel, Chaim Baskin, Evgenii Zheltonozhskii, Ron Banner, Alex M Bronstein, and Avi Mendelson. Loss aware post-training quantization. *Mach. Learn.*, 110(11):3245–3262, 2021.

- [67] Vivienne Sze, Yu-Hsin Chen, Tien-Ju Yang, and Joel S Emer. Efficient processing of deep neural networks: A tutorial and survey. *Proc. IEEE*, 105(12):2295–2329, 2017.
- [68] Amir Gholami, Sehoon Kim, Zhen Dong, Zhewei Yao, Michael W Mahoney, and Kurt Keutzer. A survey of quantization methods for efficient neural network inference. In *Low-Power Computer Vision*, pages 291–326. Chapman and Hall/CRC, 2022.
- [69] Itay Hubara, Yury Nahshan, Yair Hanani, Ron Banner, and Daniel Soudry. Accurate post training quantization with small calibration sets. In *Proc. International conference on machine learning (ICML)*, pages 4466–4475, 2021.
- [70] Xavier Glorot and Yoshua Bengio. Understanding the difficulty of training deep feedforward neural networks. In *Proc. International Conference on Artificial Intelligence and Statistics (AISTATS)*, pages 249–256, 2010.
- [71] Kaiming He, Xiangyu Zhang, Shaoqing Ren, and Jian Sun. Delving deep into rectifiers: Surpassing human-level performance on imagenet classification. In *Proc. International Conference on Computer Vision (ICCV)*, pages 1026–1034, 2015.
- [72] Yann LeCun, Léon Bottou, Genevieve B Orr, and Klaus-Robert Müller. Efficient backprop. In *Neural networks: Tricks of the trade*, pages 9–50. Springer, 2002.
- [73] Kumar Shridhar, Joonho Lee, Hideaki Hayashi, Purvanshi Mehta, Brian Kenji Iwana, Seokjun Kang, Seiichi Uchida, Sheraz Ahmed, and Andreas Dengel. Probact: A probabilistic activation function for deep neural networks. In *arxiv.org*, 2019.
- [74] Radford M Neal. *Bayesian learning for neural networks*, volume 118. Springer Science & Business Media, 2012.
- [75] Alex Wang, Amanpreet Singh, Julian Michael, Felix Hill, Omer Levy, and Samuel R Bowman. GLUE: A multi-task benchmark and analysis platform for natural language understanding. In *arXiv.org*, 2018.
- [76] Hardik Sharma, Jongse Park, Naveen Suda, Liangzhen Lai, Benson Chau, Joon Kyung Kim, Vikas Chandra, and Hadi Esmaeilzadeh. Bit fusion: Bit-level dynamically composable architecture for accelerating deep neural network. In *Proc. International Symposium on Computer Architecture (ISCA)*, pages 764–775, 2018.
- [77] Jia Deng, Wei Dong, Richard Socher, Li-Jia Li, Kai Li, and Li Fei-Fei. Imagenet: A large-scale hierarchical image database. In *Proc. IEEE Conference on Computer Vision and Pattern Recognition (CVPR)*, pages 248–255, 2009.
- [78] Ji Lin, Jiaming Tang, Haotian Tang, Shang Yang, Wei-Ming Chen, Wei-Chen Wang, Guangxuan Xiao, Xingyu Dang, Chuang Gan, and Song Han. Awq: Activation-aware weight quantization for on-device llm compression and acceleration. *Proc. Machine Learning and Systems (MLSys)*, 6:87–100, 2024.
- [79] Rajeev Balasubramonian, Andrew B Kahng, Naveen Muralimanohar, Ali Shafiee, and Vaishnav Srinivas. CACTI 7: New tools for interconnect exploration in innovative off-chip memories. *ACM Transactions on Architecture and Code Optimization (TACO)*, 14(2):1–25, 2017.
- [80] Stephen Merity, Caiming Xiong, James Bradbury, and Richard Socher. Pointer sentinel mixture models. In *arXiv.org*, 2016.